Pergamon

Journal of Structural Geology, Vol. 20, No. 9/10, pp. 1305 to 1324, 1998

0191-8141/98/$ - see front matter

PII: S0191-8141(98)00067-4

Layered granodiorites at Chebucto Head, South Mountain batholith, Nova Scotia

D. B. CLARKE

Department of Earth Sciences, Dalhousie University, Halifax, N.S., Canada, V6T 1Z4,
E-mail: clarke@is.dal.ca

and

G. K. C. CLARKE

Department of Earth and Ocean Sciences, University of British Columbia, Vancouver, B.C., Canada B3H 3J5

(*Received* 1 *July* 1997; *accepted in revised form* 20 *April* 1998)

Abstract—A sequence of more than 40 distinct, rhythmically-banded layers (typically 10–30 cm thick), occurs in the contact-zone granodiorite of the South Mountain batholith, Nova Scotia. The layered sequence shows well-developed modal mineralogical variations, grain-size variations, layer bifurcations, scour-and-fill structures, cross-bedding, slump structures, and feeder dykes. Various processes (granitization of sediments, closed-system fractionation, double-diffusion, shear flow) are incapable of explaining the field observations. Moreover, field relations suggest that the layers formed stratigraphically toward the roof of the batholith, and petrographic evidence suggests that they formed episodically from a magma of eutectoid composition. A physical model for individual layers invokes Stokes's law to describe microphenocryst settling to form the fine-grained mafic layer bottoms, and Jackson's growth rate equation to describe formation of the coarser-grained felsic layer tops. Model input variables include the initial grain sizes and their distribution in the layers, chemical diffusion rates, magma viscosities, and Newtonian or Bingham rheologies. The model predicts settling times of approximately 10 years for the microphenocrysts to form the fine-grained biotite-rich layer bottoms, and mechanical solidification times of approximately 10–25 years for the coarser-grained felsic upper parts of the layers. Thus, we believe that a coupled and repeating sequence of congealed roof-block subsidence to create space, and magma injection into that space, can account for the rhythmic layering in the granodiorite at Chebucto Head.

INTRODUCTION

Some granitoid rocks may be texturally isotropic, but most have anisotropic fabrics, developed at temperatures above and/or below the mechanical solidus (Paterson *et al*., 1989). A special subset of anisotropic fabrics is the occurrence of layers (Irvine, 1987a) showing variation in grain size and modal proportions of minerals. For decades, such layering in igneous rocks has beguiled petrologists because of its potential to reveal some of the mechanical and chemical processes that operated during the magmatic stage of development of those rocks. Led by the studies of Skaergaard and other mafic intrusions (e.g. Wager and Brown, 1967; Parsons, 1987; Cawthorn, 1996), many processes have been advanced to explain the variety of grain-sizes, modal proportions of minerals, and cryptic layering in gabbroic rocks. These include such widely varying interpretations as traditional gravity settling, deposition from turbidity currents with a component of gravity fractionation, slurry surges, two-phase convection, shear flow resulting in flowage differentiation, double-diffusive convection, liquid immiscibility, metasomatism of sedimentary rocks, and even metamorphic (solid-state) differentiation (Irvine, 1987b; Naslund and McBirney, 1996) in attempts to explain the field observations. No single process is adequate to explain all types of layers in gabbroic rocks.

Interpretations of layers in granitoid rocks are even more problematic because of higher magma viscosities and considerable uncertainties about the Newtonian or Bingham properties of silicic magmas. In general, compared with gabbroic rocks, the layers in granitoid rocks are more discontinuous, and many have been interpreted as schlieren related to shear flow, streaked-out heterogeneities, or the products of partial assimilation. Examples of detailed descriptions of layers in granitoid rocks include those of Balk (1937), Harry and Emeleus (1960), Wilshire (1969), Barrière (1981), Marre (1986), Duke *et al*. (1988), Berry and Flint (1988), and Stephenson (1990).

Smith (1975) offered a shear flow model for the layered granodiorites at Chebucto Head; however, we believe that these layers offer unusually clear evidence of the processes leading to their formation, and that a different interpretation is necessary. We believe that such structural features are the result of complex interaction of physical and chemical processes. The purpose of this paper is to provide detailed descriptions of the field relations at Chebucto Head, and to provide a mechanically and thermodynamically realistic model for the layer development.

FIELD RELATIONS

Geological setting

The South Mountain batholith outcrops over an area of 7500 km^2 in southern Nova Scotia, and is a massive, post-tectonic, peraluminous granitoid complex dominated by granodiorite and monzogranite (Clarke and Muecke, 1985). The modal mineralogy consists of quartz, plagioclase, K-feldspar, biotite, muscovite, cordierite, zircon, apatite and/or monazite, and a notable absence of Fe–Ti oxide phases. Well-developed layers occur at two localities near its eastern contact: on the coast just south of Chebucto Head (Clarke, 1980), and to a lesser extent at Pennant Point, 12 km southwest of Chebucto Head. Similar layers also occur in two satellite plutons: near the southern contact of the Musquodoboit batholith (MacDonald, 1981), and in the Port Mouton pluton (Woodend-Douma, 1988). Nowhere in Nova Scotia are layers better developed and exposed than at Chebucto Head, but Barrière (1981) has described similar features from the Ploumanac'h granite in Brittany, and Fowler *et al.* (1986) and Sisson *et al.* (1988) have described similar features from the Sierra Nevada, California. In many documented cases, the layers are within the outermost 5% of the radius of the pluton. This position may be significant in the origin of the layers.

The host rock for the layered sequence at Chebucto Head is a foliated porphyritic biotite granodiorite (Abbott, 1989) with large (up to 10 cm) megacrysts of K-feldspar and an assortment of metasedimentary xenoliths, normally ellipsoidal in shape and less than 30 cm in the major axis. The best-developed layering crops out over an area of *ca* 30 × 40 m, is *ca* 8 m thick, and dips gently to the east (Fig. 1). Other small patches of layering also occur in the vicinity, as do long thin layers that extend *ca* 200 m north of the main layered sequence. Petrologically the layered rocks are similar in modal mineralogy and overall grain size to the foliated granodiorite, except that the coarse fractions (K-feldspar megacrysts and metasedimentary xenoliths) are missing, and that both grain-size and modal mineral sorting occur in the layers.

Table 1a. Data for 18 layers having uniform thickness

Zone	Thickness range (cm)	Mean (cm)	Standard deviation (cm)
Felsic-rich top	2.0–19.0	6.9	4.7
Biotite-rich bottom	1.5–6.0	2.7	3.5

The resulting ratio of bottom/total is 0.3 ± 0.1.

Features of the layers

Lower contact of the layered sequence. The lower contact of the layered sequence against the foliated granodiorite host is planar and razor sharp (Fig. 2a). This sharpness suggests that the foliated granodiorite underwent brittle fracture; because the layers rest stratigraphically on this planar surface, the host must have behaved as a solid substrate prior to and during the layer formation event. The orientation of the layers relative to the main contact of the batholith against the country rock is unknown because that contact is offshore. However, abundant, and rarely very large, xenoliths at Portuguese Cove, 2.5 km to the northwest, suggest that this whole area may be close to the roof of the batholith. We believe that roof zones of batholiths are characterized by regions of shear flow where magmas move past static walls, and by steep temperature gradients. Either of these factors may be important in developing conditions suitable for forming layers.

Table 1b. Modal compositions of source region and layers based on more than 1100 points counted per sample (volume %)

Component	Layer top		Layer base		Unlayered pluton	
	(a)	(a′)	(b)	(b′)	(c)	(c′)
Quartz	35	37	24	37	32	37
Plagioclase	42	44	29	45	39	45
K-feldspar	18	19	12	18	16	18
Biotite	5	—	35	—	13	—

Columns (a′), (b′), and (c′) are computed with biotite removed.

Table 1c. Typical crystal radius in source region and layers (mm)

Component	Layer top (a)	Layer base (b)	Unlayered pluton (c)
Quartz	2.5	1.0	3.0
Plagioclase	2.5	1.0	5.0
K-feldspar	2.5	1.0	50*
Biotite	2.5	1.0	3.0

*Phenocrysts.

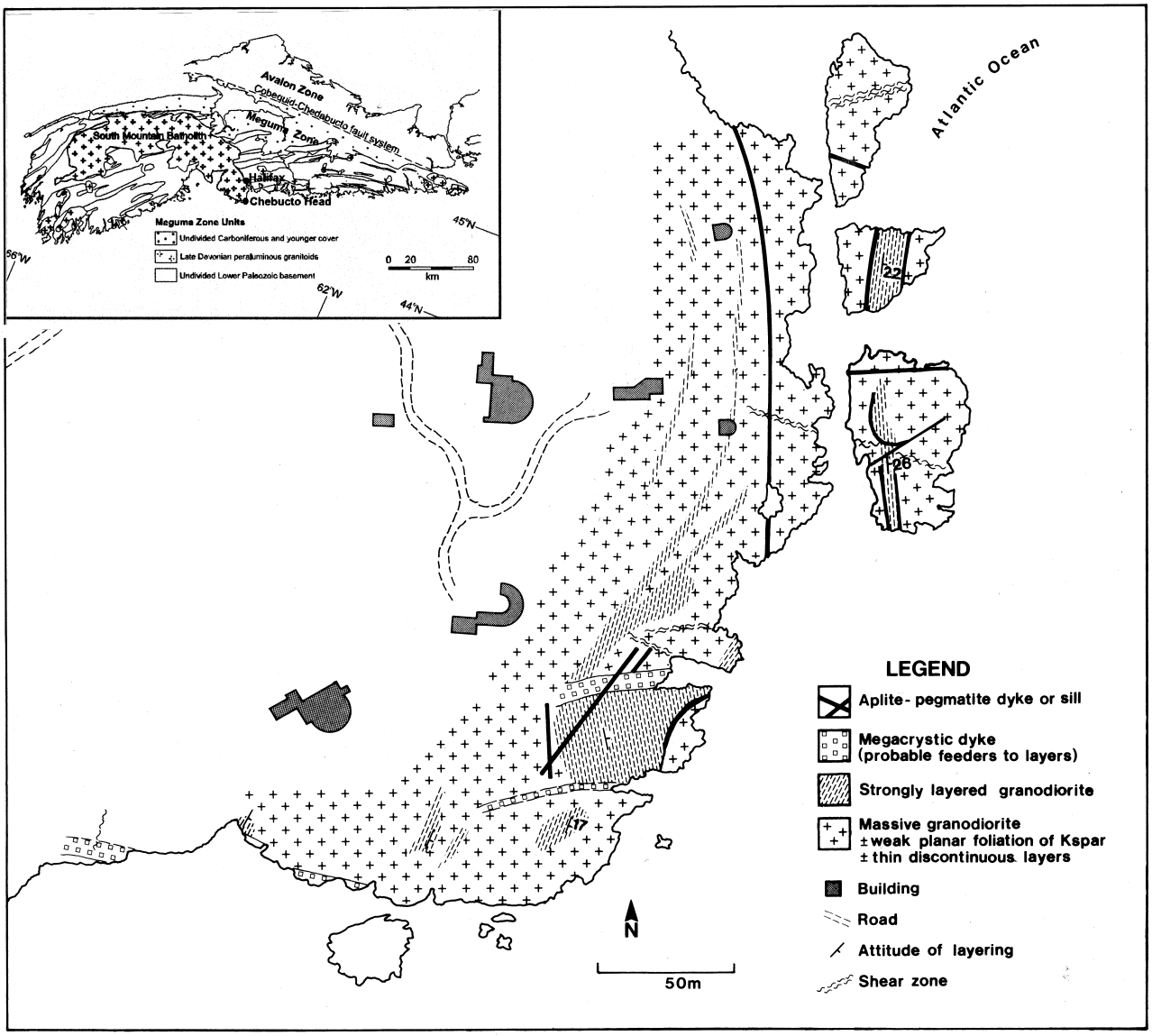

Fig. 1. Map of the layered sequence at Chebucto Head, Nova Scotia. The thickest and best developed sequence of layers is confined between two megacrystic dykes in the south, but thinner sequences of layers extend to the north and also occur on two of the small islands. Inset: location of Chebucto Head in southern Nova Scotia.

Rhythmic layering. The layered sequence consists of more than 40 distinct layers that characteristically have type B rhythmic banding (sudden change followed by gradual return to original conditions (Nasland and McBirney, 1996)). The rhythmic units average 20 cm in thickness (range 5–50 cm) (Fig. 2b). Each rhythmic unit begins at the base with a sharp contact against the layer below, and consists of a fine-grained biotite-rich (up to 35%) bottom overlain by a coarser, biotite-poor (< 10%) top (Table 1a). Plagioclase crystals in the bottom are homogeneous except for narrow rims, whereas plagioclase grains in the top are strongly zoned from core to rim. This consistent polarity suggests that some regular process (gravity sorting? shear flow?) operated repeatedly. If gravity sorting; whether the small biotite crystals could ever have settled to the bottoms of the layers, before the layers themselves solidified, is a pivotal question. If shear flow; why is the present distribution of grain size asymmetrical?

Foliation without lineation. As mentioned previously, the rhythmic layers are largely free of coarse constituents; some of the lowermost layers, however, contain tabular K-feldspar megacrysts at the bottoms of the rhythmic units. These feldspars normally have good planar foliation, with their (010) faces lying parallel to the base of the layers (Fig. 2c). On outcrop surfaces parallel to the plane of the layering, the long axes of the K-feldspar phenocrysts show no preferred orientation (Fig. 2d). Such a distribution of megacrysts within the layers, and their random orientations, appear to be more consistent with gravity-controlled settling than shear flow.

Layer bifurcation. Many of the rhythmic layers are reasonably parallel, but in several places these layers split into two or more branches (Fig. 2e & f). Layer

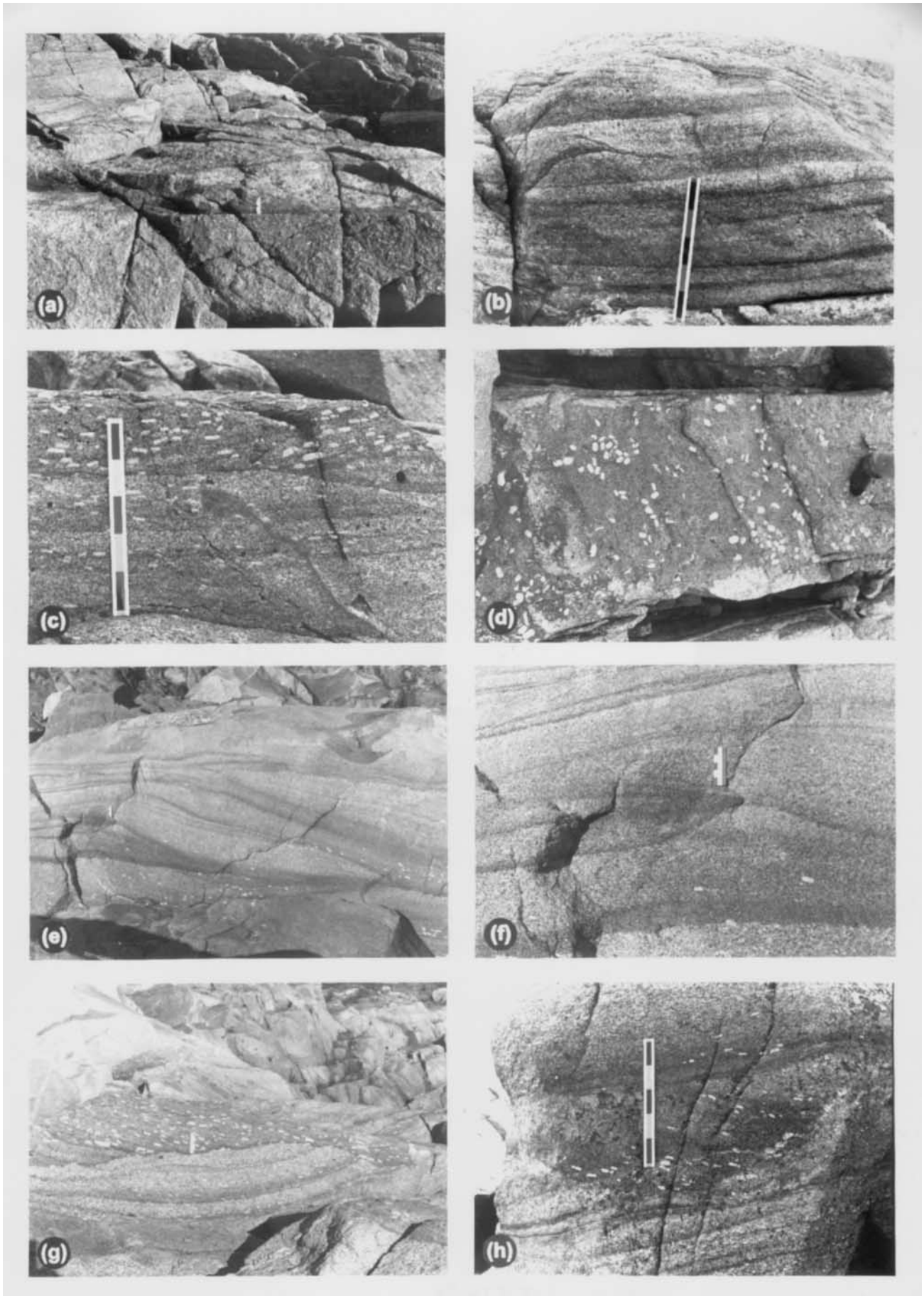

Fig. 2(a–h). *Caption on p. 1310.*

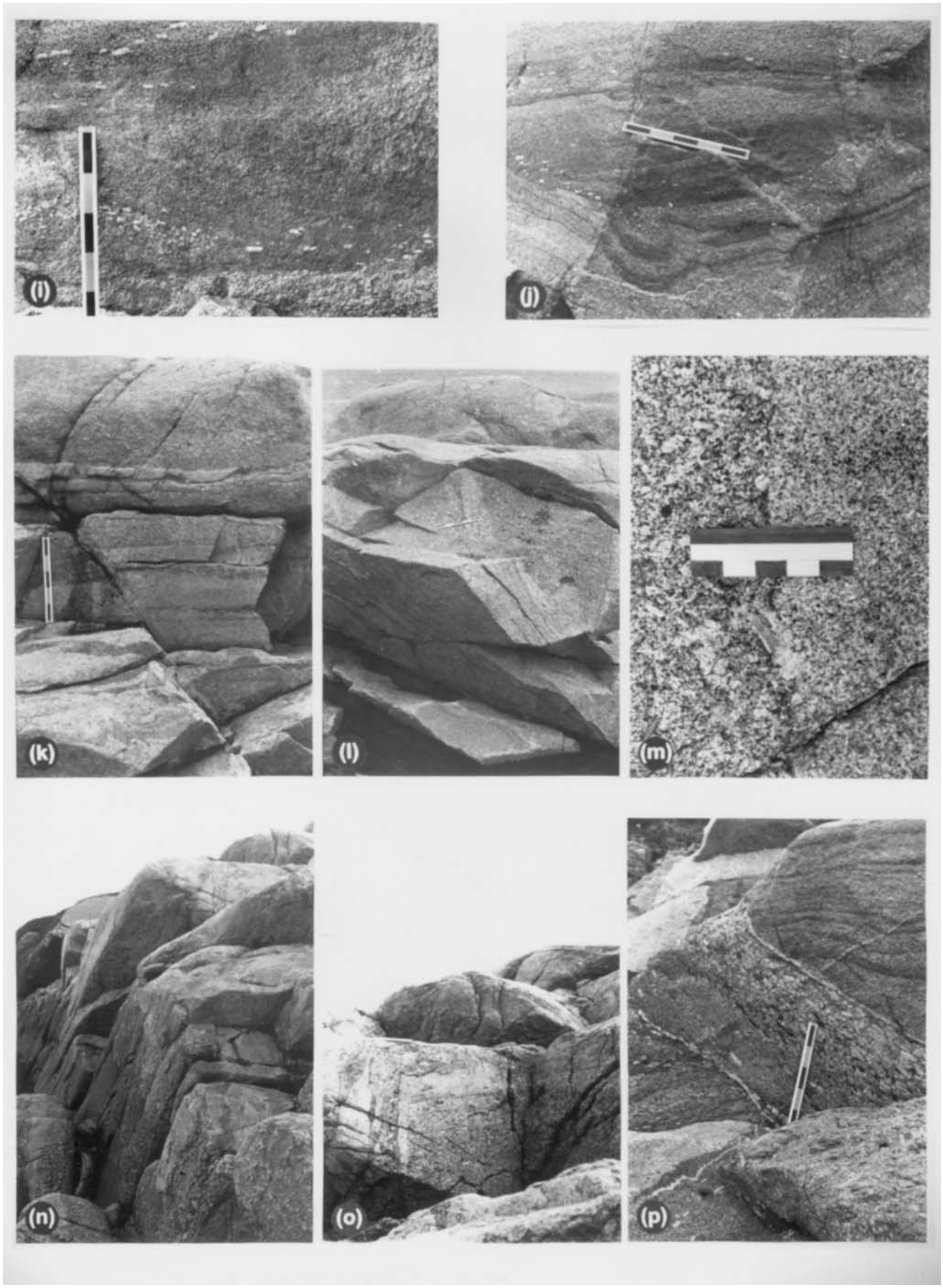

Fig. 2(i–p)—*caption overleaf*.

branching occurs in many other plutons (Balk, 1937; Wilshire, 1969; Parsons, 1987) and is invariably a source of controversy. In clastic sedimentary sequences, branching layers may simply represent pinching out of one or more of the individual units, and the same principle may apply in igneous rocks.

Trough structures. Well-developed trough or channel structures, resembling scour-and-fill structures in clastic sedimentary rocks, occur within the layered sequence (Fig. 2g & h). In every case, material appears to have been removed from the topographically lower layers, but not from the overlying layers. Using sedimentological criteria, all trough structures demonstrate that the layered sequence is right-way up, suggesting that it was constructed upwards toward the roof of the batholith. A second important inference from the channel structures is that fresh material to form new layers intruded before one or more of the immediately preceding layers had acquired complete mechanical integrity.

Cross-bedding. In one locality, foliated biotite flakes and a few of the K-feldspar megacrysts show well-developed cross-bedding resembling foreset beds (Fig. 2i). In terms of classical sedimentology, the cross-bedded unit is an advancing foreset bed; alternatively, the foliation of biotite and K-feldspar megacrysts is simply parallel to the margin of a deeply-incised channel running perpendicular to the present vertical outcrop surface.

Deformed layers. In three places, several layers have apparently deformed together into concentric folds (Fig. 2j). Layers above and below appear not to have been affected by the deformation process. That only a few layers are affected suggests that the deformation process must have operated during, rather than after, the construction of the layered sequence. Sedimentologically, the deformed layers might be slump structures. Their restriction to a few horizons suggests that, at the time deformation occurred, only the most recently formed and hence weakest layers were affected. This view is consistent with conclusions based on examination of the scour-and-fill structures: the time between successive layer-formation events was normally less than the time necessary for complete solidification of a layer. Brown *et al*. (1987) arrived at the same conclusion for a large 'soft-sediment' fold in the Lilloise intrusion of East Greenland.

Upper contact of the layered sequence. The upper contact of the layered sequence is sharp against the foliated granodiorite host, but this contact is complicated by several aplitic injections (sills) parallel to the contact in the upper metre of the layered sequence (Fig. 2k). Even if the complexities of the late aplitic sheets are removed, the leucocratic portion of the uppermost layer may be anomalously thick. Also, this upper contact is subparallel to the one at the base, and we take this parallelism as strong evidence that the entire layered sequence developed episodically within a single widening subhorizontal fracture.

In addition to the features of the layers themselves, the following two associated features may be relevant to the formation of the layers.

Diapiric structure. A conical diapir protrudes upward from the layered sequence, into the overlying foliated granodiorite (Fig. 2l), and consists of material free of phenocrysts and xenoliths, indistinguishable from the layer material. The importance of this diapir is that it contains information about the timing of layer emplacement, the relative viscosities of the layered sequence and the enclosing foliated granodiorite, and

Fig. 2. Field observations of the layers at Chebucto Head. (a) The lower contact of the layered sequence. Note that the contact between the lower boundary of the layered sequence (above) and the foliated host granodiorite (below) is sharp. The entire length of the scale is 10 cm. (b) Rhythmic layering. More than 40 distinct layers occur, with a typical layer thickness of 15–20 cm. The layers are biotite-rich at the base and grade upward to biotite-poor and quartz–feldspar-rich. Each major division on the scale represents 10 cm. (c) Foliated tabular K-feldspar megacrysts, with (010) faces parallel to the base of the layer, in the lowermost layers of the layered sequence. With the exception of the lowermost layers, the rhythmic layers are generally free of coarse constituents. (d) View looking down on surface of layering shows no lineation of the long axes of the feldspar crystals. Human foot for scale. (e) Layer bifurcation. (f) Enlarged portion of previous photograph. Entire scale length is 10 cm. (g) Scour-and-fill structure. Overlying dark layer truncates lower rhythmic layers on left and right of photograph. Entire scale length is 10 cm. (h) Deeply scoured channel (in centre of photograph) cutting through several rhythmic layers. Each major division on the scale represents 10 cm. (i) Cross-bedding in the layered sequence. Beds resembling foreset beds are defined by foliated biotite flakes and K-feldspar megacrysts. Each major division on the scale represents 10 cm. (j) Layers that appear to have deformed together into concentric folds. Layers above and below appear unaffected by the deformation process. Each major division on the scale represents 10 cm. (k) Top of the layered sequence showing a sharp contact between the uppermost layer and the foliated granodiorite above it. The contact is complicated by several aplitic injections parallel to the contact in the upper metre of the layered sequence. Each major division on the scale represents 10 cm. (l) Diapiric structure (lighter-coloured material under the scale) protruding upward from the layered sequence into the overlying foliated granodiorite. The diapiric material has a composition similar to that of the layers and is free of phenocrysts and megacrysts. Each major division on the scale represents 10 cm. (m) Enlarged portion of previous photograph showing foliated granodiorite (on the left) in contact with fine-grained homogeneous diapiric material (right). Below the scale is a large K-feldspar phenocryst lying across the contact. Each major division on the scale represents 10 cm. (n) Part of the megacrystic dyke bounding the north side of the layered sequence (Fig. 1). In the lower left are indications of the composite nature of the dyke, and also the high concentration of K-feldspar phenocrysts. The 10 cm scale (full length) in upper right marks the transition from vertical dyke to horizontal layer detailed in (o). (o) Enlargement of previous photograph showing detail of dyke-to-layer transition. The lowermost layers are visible on the right-hand side of the photograph. (p) Sinuous megacrystic dyke cutting through the layered sequence. Each major scale division is 10 cm.

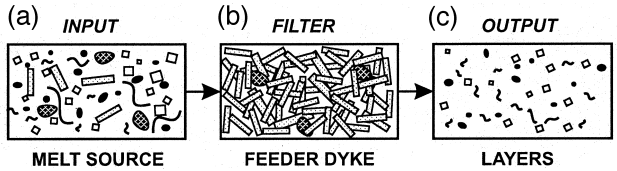

Fig. 3. Input–output system. (a) Melt in the source region contains a mixture of K-feldspar megacrysts (large rectangles) and xenoliths (large dark ellipsoidal blobs) as well as microphenocrysts of felsic minerals (small white squares), biotite (small black ellipses), and long polymeric chain molecules in the melt phase (black worm-like curves). (b) The feeder dyke is clogged with a log-jam of megacrysts and xenoliths. (c) Melt that is transmitted from the source region to the layers is filtered through the feeder dyke. The effects of this sieving process are to remove megacrysts and xenoliths, to break down long polymeric chains into shorter chains, and to pass melt-suspended felsic and mafic microphenocrysts.

the upward direction for the layered sequence. This diapirism demonstrates not only the low viscosity of the upper layers, but also the plasticity of the overlying granodiorite when subjected to long-term stress. To create the initial space for the layers, the overlying granodiorite must have undergone brittle fracture as a high strain rate response to some other stress (e.g. gravity, thermal contraction) but, after the layers formed, it underwent ductile deformation. In one place, a large K-feldspar megacryst lies astride the contact with the foliated granodiorite (Fig. 2m). Smith (1975) suggested that this K-feldspar megacryst was evidence that all the megacrysts in the area were metasomatic in origin. However, a metasomatic origin fails to explain their general absence from the layered sequence, their foliation when they do occur, their abundance in the megacrystic dykes, and their observed concentric zones of inclusions of other magmatic phases (quartz, plagioclase, biotite). On the contrary, the megacryst lying across the diapir contact is probably just one of the normal magmatic constituents of the foliated granodiorite that was in the process of being included in the diapir as it ascended into the overlying foliated granodiorite.

Cross-cutting dykes. Three types of cross-cutting dykes occur within the layered sequence. One type is a set of late-stage aplites that cut all other lithological types in the area (Fig. 1) and are not involved in the layer-formation process. A second type consists of two dykes striking roughly east–west and forming the boundaries of the well-developed layered sequence. These dykes have high concentrations of K-feldspar phenocrysts (mapped as megacrystic dykes on Fig. 1), and the dykes show zoning defined by well-developed internal vertical contacts between material having varying concentrations of feldspar phenocrysts and biotite (Fig. 2n). At one important location, the outer margin of the large megacrystic dyke 'bends' by 90° to become the lowermost layer (Fig. 2o). The main megacrystic dyke does not extend topographically or stratigraphically higher than the uppermost layer of the layered sequence as indicated by its coincident and apparent termination to the west of the layered sequence (Fig. 1). The genetic importance of the megacrystic dykes is indicated by several lines of evidence: (i) their close spatial relationship to layered rocks; (ii) their high content of K-feldspar megacrysts, a mineralogical constituent depleted in the layers; (iii) the composite nature of the main dyke—suggesting that it has been episodically-active and that these episodes may also correspond to layer-formation events; (iv) the remarkable 90° bend in the main dyke suggesting a classical feeder relationship between dyke and layers; and (v) the main dyke does not extend higher than the layered sequence. The last two points are particularly important in demonstrating that at its apex the dyke transformed into a sheet, and that the resulting sheet had sharp upper and lower contacts. Finally, a third type of dyke within the layered sequence (not shown on Fig. 1) has sharp contacts within the layers, contains a very high concentration of K-feldspar phenocrysts and xenoliths (Fig. 2p), and in some places cuts the layers at high angles whereas in other places it is almost sill-like. We defer discussion of this dyke to a subsequent section.

In summary, the field relations suggest that the layers formed by sequential sill-like injections of magma. We address the feasibility of gravity settling as a mechanism to produce the modal and grain size variations of the layers in the next section.

PHYSICAL MODEL

Overview

In this section we develop a physical model to describe the thermal, chemical, and structural evolution of a single layer. Schematically, the source region, feeder dyke, and layers can be viewed as an input–output system which transfers melt and solids from the source region to the layers above (Fig. 3). The feeder dyke serves as a mechanical sieve which filters out large crystals, passing only smaller crystals and melt. Our model concentrates attention on the layers and does not attempt a quantitative description of the processes operating in the source region or feeder dyke. Episodic repetition of this layering process would result in a stack of layers such as that observed (Fig. 2b).

The main features of the model are summarized in Fig. 4. (i) Immediately after creation of a slot-like void, melt and solids are extracted from the source region to fill this void with a random suspension of

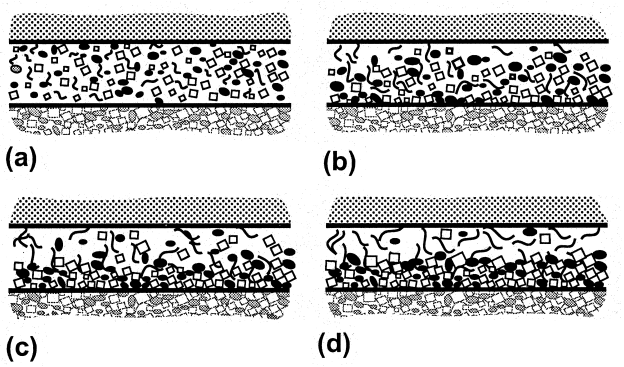

Fig. 4. Process summary for a representative layer of the layered sequence. The layer on top consists of country rock and the bottom of material from the previously-deposited layer. Felsic crystals are indicated by white squares, biotite by black ellipses, and polymeric chain molecules by black worm-like curves. (a) Immediately after creation of a slot-like void space, a random suspension of microphenocrysts invades the slot. (b) Biotite crystals settle more rapidly than felsic crystals of comparable size and become concentrated at the layer bottom. (c) Grain growth and crystal settling proceed concurrently. (d) Progressive melt polymerization impedes crystal settling and allows some crystals to grow large before they settle or have their settling arrested by Bingham forces.

crystals. The grain-size distribution of these suspended crystals will differ from that of the source region because the feeder dyke only passes small crystals. The sieving process is purely mechanical, so the initial grain-size distribution for all solid phases in the layer is assumed to be identical, although the relative abundances of the various mineral species differs. For all layers after the first, the layer substrate is formed by material deposited in the layer immediately preceding it (Fig. 4a). (ii) Biotite is the most dense solid phase and, despite its unfavourable shape, settles more rapidly than felsic minerals of comparable size. As sedimentation of biotite and felsic minerals proceeds, crystals accumulate at the lower boundary of the layer and a solids-depleted zone forms at the upper boundary (Fig. 4b). (iii) Grain growth and crystal settling proceed concurrently. Growth of settled crystals is inhibited by neighbouring grains. Suspended crystals do not have this limitation, but the larger such crystals grow, the greater their settling rate (Fig. 4c). (iv) The presence of large felsic crystals near the upper boundary of layers indicates that some process counteracts the tendency of growing crystals to settle to the layer bottom. We propose that the process that inhibits this settling is melt polymerization (Fig. 4d).

Assumptions of the model

Source. The temperature and chemistry of the layer-forming material are largely determined by characteristics of the source region. On this basis we infer the following: (i) The melt for both the source and layers is saturated with all the main mineral phases (plagioclase, K-feldspar, quartz, and biotite) but minor phases (e.g. H_2O, aluminosilicate, cordierite, and trace minerals) are undersaturated in the melt. Thus, the temperature of the source region is near the solidus temperature and the melt composition is cotectic. (ii) A more detailed analysis using our computer model shows that the characteristic time for layers to reach chemical and thermal steady state is 10–15 years. Thus, relatively, the thermal and chemical evolution of the main part of the batholith proceeds so slowly that the temperature and chemistry of the source material can be regarded as constant for each individual layer-forming event. (iii) A consequence of the slowness of the thermal and chemical processes in the pluton is that solid and melt phases in the source region are near chemical equilibrium with each other. Thus, in the source region, the amount of undercooling is very small, as are the rates of crystal nucleation and growth.

The foregoing inferences place strong constraints on the temperature and chemistry of the melt input to layers. For simplicity we shall represent the melt as a ternary system and denote the components as A, B, and C. Component A comprises all felsic components (plagioclase, K-feldspar, and quartz), component B represents the mafic component (biotite), and component C represents all minor constituents including water (Fig. 5). The positions of the cotectic lines and eutectics are based on experimental observations (Abbott and Clarke, 1979; Vielzeuf and Holloway, 1988; Peterson and Newton, 1988). The chemical evolution of the layers is assumed to lie on the cotectic line AB–E and the superimposed isotherms indicate the assumed effect of composition on liquidus temperature. The initial temperature of the layer-forming material

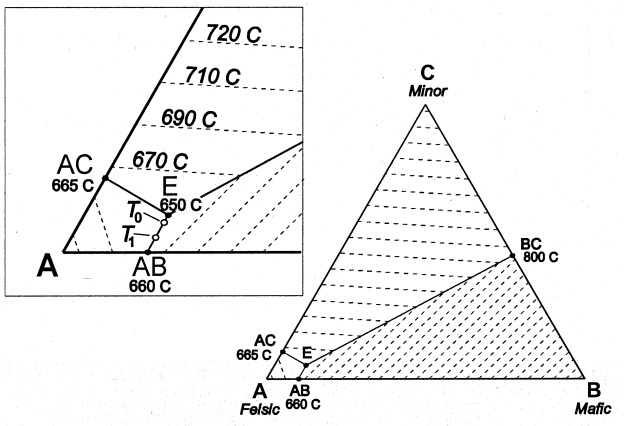

Fig. 5. Ternary phase diagram. Felsic components are collectively represented by A; mafic components (biotite) by B; minor constituents by C. Compositions are expressed in terms of the *volume* concentrations of the melt components. The binary and ternary eutectic points are denoted AB, BC, CA, and E. Isotherms of the melt liquidus temperature are contoured. The geometry of this temperature surface is fixed by the compositions associated with each of the eutectic points and a specification of the liquidus temperature at each of these points. *Inset*. Details of the phase diagram in the compositional region relevant to our model. The melt is assumed to have a cotectic composition defined by the line AB–E. The initial composition corresponds to the initial melt temperature T_1 and the final composition corresponds to the ambient temperature T_0 (open circles on AB–E).

T_1 and that of the cooler surroundings T_0 are indicated on the AB–E line (inset Fig. 5).

Feeder dyke. During layer-formation events, the phenocryst-choked dyke (Fig. 2n & o) delivers magma from the source region to the layers, but the passage of large crystals to the layers is inhibited by the log-jam of phenocrysts. The effect is to alter the size distribution so that solids injected to the layers have smaller average grain size than those in the source region. The sieving process is entirely mechanical and in this case selection takes place primarily on the basis of grain size. Thus, in the layers the initial size distributions, although not the relative abundance, of all solid phases is identical. Our second role for the feeder dyke is speculative. We stated above that melt in the source region is extensively polymerized; we postulate that the sieving process depolymerizes melt that is injected into the layers. The process that could effect this depolymerization is chain scission, well known to polymer science (Rodriguez, 1982). Essentially, it is the mechanical cutting of long polymeric chains into shorter ones and it is a plausible consequence of the very large strain rates associated with sieving the melt through the feeder dyke. Melt depolymerization has rheological implications. A highly-polymerized melt might be expected to have a yield strength and behave like a Bingham fluid. A depolymerized melt would have little or no yield strength and behave like a Newtonian fluid.

Layers. Turning attention to the layers, the following observations are germane to the modelling. (i) The layers are situated stratigraphically above the source region, suggesting that the ambient temperature in the vicinity of the layers is less than the source temperature. If the upper boundary of the pluton is at a depth of 10 km (Clarke and Muecke, 1985) and at ~650°C the average geothermal gradient above the pluton is ~0.065° m^{-1}. Thus, if the layers were situated ~50 m above the pluton the ambient temperature there would be ~3.25°C lower than the source temperature. It does not seem plausible that the layered zone lies far above the molten part of the pluton because this would place the feeder dyke in thermally-unfavourable surroundings and would promote its solidification. (ii) All the solid phases in the material injected into the layers are more dense than the melt phase. Some degree of crystal settling should therefore occur. (iii) The thermal environment of the layers is cooler than the initial temperature of the layer-forming material from the source region. Once the injected magma has cooled to near the ambient temperature, this layer-forming material will be undercooled. Thus crystal growth and nucleation are potentially significant processes. (iv) The short-term mechanical disruption that accompanies layer formation and melt injection is followed by much longer intervals during which crystal settling is the only mechanical process in operation. During these intervals the melt and solid phases in the layers evolve toward thermal, chemical, and mechanical equilibrium and the melt phase again becomes extensively polymerized. As polymerization proceeds, the Bingham yield stress of the melt increases. The effect of this is to interfere progressively with the crystal settling process and to strand some crystals before they can settle to the layer bottom. In our modelling this postulated yield strength is very small so its only influence would be to inhibit crystal settling; there would be no observable effect on large-scale fluid mechanical processes.

Our final category of modelling assumptions are those motivated by computational rather than geological or physical considerations. Of these, the most important is our assumption that volume, rather than mass, is a conserved quantity. In nature, a liquid-to-solid phase change is accompanied by volume change, but the mass of substance remains constant. In our model we assume that a density change occurs but that volume remains constant. This assumption leads to profound simplifications in the computational model, but we believe it is innocent in terms of its effect on the essential physics of the model. A second expedient assumption is that the heat capacity ρc is identical for the melt and all solid phases. This assumption greatly simplifies the modelling of thermal evolution without compromising the physics. Finally, we must assume initial size distribution functions for each of the solid phases and, further, to assume the spatial distribution functions for solid particles within the layer. We have assumed that the felsic (A) crystals and the mafic (B) crystals in the layers have identical Gaussian size distributions. In terms of the spatial distributions, we have chosen to make the simplest assumption—that the distribution is spatially uniform. It would be straightforward to assume something more complicated, for example that flowage differentiation (Bhattacharji and Smith, 1964) would concentrate large crystals near the layer mid-plane, but any such approach would require additional justifications. Furthermore, we contend that the final structure of the layers can develop from an unstructured initial state and is a natural consequence of the physical processes operating in the layers.

Physics of the model

In our model we are concerned with thermal, chemical, and mechanical phenomena operating in a horizontal layer of thickness h bounded above and below by a uniform semi-infinite thermally-conducting solid. We choose a coordinate system such that the z axis is vertical and positive upward with x and y coordinates indicating horizontal position. The layer boundaries are at $z = 0$ and $z = h$. Initially the layer contains melt and solids at temperature T_1 and the surroundings are at temperature T_0. The thermal properties of the layer materials and the surroundings are assumed to be identical; thus for the walls, crystals, and melt,

ρc is the heat capacity, K is the thermal conductivity, and $\kappa = K/\rho c$ is the thermal diffusivity.

At the onset of a layer-formation event, the injected material is a mixture of felsic and mafic crystals suspended in a melt. Individual crystals, labelled by an index p, have attributes such as composition e_p where $e_p = A$ or $e_p = B$ depending on whether the crystal is felsic or mafic, spatial position (x_p, y_p, z_p), radius r_p, and density ρ_p. The melt has properties such as temperature T and composition c_α. For mathematical convenience, we shall express chemical concentrations as volume fractions of the pure melt components, i.e. c_A, c_B, and c_C where $c_A + c_B + c_C = 1$. In our model, temperature and composition are taken to vary with vertical position z and time t, where $t = 0$ at the instant that layer injection occurs.

Crystal settling is assumed to be governed by Stokes's law but with adjustments for non-spherical crystal shape (Lamb, 1963), grain cluttering (Maude and Whitmore, 1958), and Bingham behaviour of the melt. Appendix A gives details. For a particle p of density ρ_p located at the point having (x_p, y_p, z_p, the rate of change of vertical coordinate with time is taken as

$$\frac{dz_p}{dt} = -v_p \tag{1a}$$

where

$$v_p = \begin{cases} v_p^S - v_p^B & v_p^S > v_p^B \\ 0 & v_p^S \le v_p^B \end{cases} \tag{1b}$$

with

$$v_p^S = \begin{cases} \dfrac{2}{9\mu_E}\left(\rho_p - \rho_m\right) g r_p^2 & \text{for spheres} \\ \dfrac{\Gamma\pi}{13.06\mu_E}\left(\rho_p - \rho_m\right) g r_p^2 & \text{for disks} \end{cases} \tag{1c}$$

and

$$v_p^B = \begin{cases} \dfrac{2\tau r_p}{3\mu_E} & \text{for spheres} \\ \dfrac{2\pi(1+\Gamma)\tau r_p}{13.06\mu_E} & \text{for disks} \end{cases} \tag{1d}$$

with

$$\mu_E = \begin{cases} \mu/m^{4.65} & m > m_0 \\ \mu/m_0^{4.65} & m \le m_0 \end{cases}. \tag{1e}$$

In the above equations v_p is the crystal settling velocity, v_p^S and v_p^B are velocity functions relating to Stokes and Bingham behaviour, g is the gravity acceleration, μ_E is an effective viscosity associated with grain cluttering, Γ is the thickness-to-volume ratio for a circular disk having radius r_p, τ is the Bingham yield stress for the melt, and m_0 is the volume fraction of melt that corresponds to the solid packing density in a freshly-sedimented layer. We assume a temperature-dependent melt viscosity such that

$$\mu(T) = \mu_0 \exp\left\{ QR\left(\frac{1}{T} - \frac{1}{T_R}\right)\right\} \tag{2}$$

where T is absolute temperature, μ_0 is a reference value for viscosity, Q is an activation energy, and $R = 8.31434$ J mol^{-1} K^{-1} is the gas constant. Felsic crystals are assumed to be spheres of radius r_p whereas biotite crystals are treated as circular disks having radius r_p and thickness Γr_p where Γ is a dimensionless aspect ratio. The Bingham yield stress is assumed to vary according to

$$\tau = \tau_\infty + (\tau_0 - \tau_\infty)\exp(-t/t_B) \tag{3}$$

where τ_∞ is the value of yield stress in the long-time limit, τ_0 is the initial value (we take this as zero), and t_B is a time constant. (See Appendix B for additional discussion concerning the basis of equation (3).)

Crystal growth is modelled using Jackson's (1967) equation

$$\frac{dr_p}{dt} = \frac{1}{\mu}\left[1 - \exp\left(-\frac{H_p \Delta T}{RT T_L}\right)\right] V_p \tag{4}$$

where H_p is the enthalphy of melting, $\Delta T = T_L - T$ is the undercooling, and V_p is the reduced growth rate. The choice of enthalpy and growth rate depends on the composition of the particular crystal. In our system we consider only two solid phases. Thus if $e_p = A$, we take $H_p = H_A$ and $V_p = V_A$; if $e_p = B$, we take $H_p = H_B$ and $V_p = V_B$. In equation (4), the temperature T_L represents the compositionally-dependent liquidus temperature $T_L = T_L(c_A, c_B, c_C)$ as illustrated in Fig. 5. We impose the additional reasonable restriction that growth of any solid phase can only proceed when the melt composition lies in the appropriate field of the ternary diagram. On the AB–E cotectic line, two solid phases can grow and, in our model, this growth is achieved by macroscopically-imperceptible excursions back and forth between fields A and B. Thus, at any given time and position only one solid phase is actively growing. In equation (4), growth of all crystals stops when $T = T_L$; thus growth of large crystals at the expense of small ones (e.g. Boudreau, 1995; Boudreau and McBirney, 1997) is not a possibility.

Crystal nucleation is modelled using the following equation, slightly-modified from that derived by Turnbull and Fischer (1949) and commonly applied to geological calculations (e.g. Dowty, 1980; Brandeis *et al.*, 1984):

$$\frac{dn'_\alpha}{dt} = mK_\alpha^{(1)} T \exp\left(-\frac{K_\alpha^{(2)}}{(T_L - T)^2 T}\right)\exp\left(-\frac{K_\alpha^{(3)}}{T}\right) \tag{5}$$

where n'_α is the number density of crystals having composition α and $K_\alpha^{(1)}$, $K_\alpha^{(2)}$, $K_\alpha^{(3)}$ are experimentally-determined rate constants appropriate to solid phase α. The multiplicative factor m is inserted to express the fact

that nucleation can only occur in the melt phase. Furthermore, we assume that nucleation of solid phase α can only occur when the melt composition lies in the α field of the ternary phase diagram. Thus, for example, component C cannot nucleate if the melt composition lies on the AB–E cotectic line in Fig. 5.

The thermal evolution equation is

$$\overline{\rho c}\frac{\partial T}{\partial t} = K\frac{\partial^2 T}{\partial z^2} + \sum_{\alpha} \rho_\alpha H_\alpha \Phi_\alpha \qquad (6)$$

where the subscript α identifies the mineral composition, ρ_α is the solid phase density, and H_α is the enthalpy of the phase change. The term Φ_α is the volume rate of production of solid phase α and varies both temporally and spatially. In addition to assuming a single value for heat capacity ρc and thermal conductivity K, we neglect advective heat transport by the settling crystals. This assumption is appropriate when settling rates are small, as they are for all models that we have explored.

For each melt component, the chemical balance equation takes the form

$$m\frac{\partial c_\alpha}{\partial t} = -m v_{\mathrm{m}}\frac{\partial c_\alpha}{\partial z} + \frac{\partial}{\partial z}\left(D_\alpha m^{\mathrm{v}}\frac{\partial c_\alpha}{\partial z}\right) - \Phi_\alpha + c_\alpha \sum_{\alpha}\Phi_\alpha \qquad (7)$$

(see Appendix C for a detailed derivation).

Computational strategy

An essential feature of the system that we wish to analyze is the coexistence of smoothly-varying continuum properties such as $T(z,t)$ and $c_\alpha(z,t)$ with the properties of discrete particles which, at least at local scale, have individual attributes such as chemical identity e_{p}, position $(x_{\mathrm{p}}, y_{\mathrm{p}}, z_{\mathrm{p}})$, and radius r_{p}. Intermediate between these extremes are properties such as $m(z, t)$, $\phi_\alpha(z, t)$, and $n'_\alpha(z, t)$ which present themselves as continuum properties, but are statistical properties of the ensemble of discrete particles. In the many-particle limit, these become smoothly-varying functions of space and time and the continuum approximation becomes appropriate. This is the classic approach of mathematical physics but it does not necessarily lead to the simplest calculation method. Our computational strategy is to focus on the behaviour of individual particles and, by making the number of such particles very large, estimating the smooth averages by adding over the appropriate particle ensemble. Although this method is computationally intensive, the alternative of solving the coupled systems of partial differential equations is both computationally intensive and conceptually challenging. We apply this particle-based approach to estimate $n'_\alpha(z,t)$, ϕ_α, Φ_α, and the volume flux of solids J_α. (Details are in Appendix D.) Once ϕ_α and J_α have been estimated, the volume fraction of solids $\phi_{\mathrm{s}} = \phi_{\mathrm{A}} + \phi_{\mathrm{B}} + \phi_{\mathrm{C}}$, volume fraction of melt $m = 1 - \phi_{\mathrm{s}}$, and melt velocity $v_{\mathrm{m}} = -(J_{\mathrm{A}} + J_{\mathrm{B}} + J_{\mathrm{C}})$ are readily calculated. Temperature and composition are treated as true continuum properties. Equations (6) and (7) are expressed in finite-difference form and solved using a standard Crank–Nicholson scheme (e.g. Richtmyer and Morton, 1967).

MODELLING RESULTS

The thermal, mechanical, and chemical evolution of a single layer was modelled for a 25-year period. The initial number of solid particles was $N = 100{,}000$ with the assignment of felsic and mafic proportions guided by Table 1b(b). Geological and physical input data for the model are summarized in Table 2 and thermodynamic relations for the melt are depicted in Fig. 5. The initial melt composition was assumed to lie on the AB–E cotectic line of Fig. 5 which joins the point AB (with $T_{\mathrm{L}} = 660^\circ$C) to the eutectic point E (with $T_{\mathrm{L}} = 650^\circ$C). The initial temperature of the melt is $T_1 = 656^\circ$C and that of the surroundings is $T_0 = 652^\circ$C (these temperatures are indicated by open circles along the AB–E line of Fig. 5 inset). Under these conditions, complete solidification of the layer cannot occur and the maximum possible undercooling is only $\Delta T = T_1 - T_0 = 4^\circ$C. In running the model with the nucleation rate parameters of Table 2, we found that no new crystals were nucleated; thus N remained constant throughout the simulation and processes such as oscillatory nucleation (Hort *et al.*, 1993) play no role in forming the layers.

The most striking feature of a single rhythmic layer is the decrease in the proportion of biotite coupled with the increase in grain size from bottom to top. Figure 6(a–e) illustrates several time slices of a numerical model that qualitatively matches these variations. Plotted results are given for $t = 0$, 1, 2, 5, 10, 25 years (see legend accompanying Fig. 6). The model shows a relatively rapidly growing layer of fine-grained material near the base (0–4 cm in Fig. 6a–c), consisting of the microphenocrysts which passed through the filter of the log-jam dyke. Overlying this basal zone is a layer of more felsic material (4–23 cm in Fig. 6a–c) in which growing crystals become trapped by the increasing Bingham resistance and grow to a larger grain size over a longer period of time. Above this region dominated by felsic solids lies an upper layer of crystal-poor melt (23–40 cm in Fig. 6a–c). Figure 6(b) shows that mafic solids (biotite) are concentrated near the layer base, in clear agreement with observations. The vertical variation of crystal size (Table 1c) is qualitatively reproduced by the model. At 10 y, the mean radius of felsic crystals is 1.15 mm at the layer base, increasing to 1.6 mm at 20 cm above the base (Fig. 6d); for biotite the mean radius increases from 1 to 1.25 mm over the same distance range (Fig. 6e). At 25

Table 2. Summary of modelling data

Physical property	Value
Layer thickness, h	0.40 m
Initial temperature of surroundings, T_0	652°C
Initial temperature of layer, T_1	656°C
Density of felsic crystals, ρ_A	2650 kg m^{-3}
Density of mafic crystals, ρ_B	3200 kg m^{-3}
Density of melt, ρ_m	2450 kg m^{-3}
Thickness-to-radius ratio for biotite crystals, Γ	0.5
Initial mean radius of felsic crystals, $r_A(0)$	0.75 mm
Initial mean radius of mafic crystals, $r_B(0)$	0.75 mm
Initial radius standard distribution for felsic crystals, $\sigma_A(0)$	0.25 mm
Initial radius standard distribution for mafic crystals, $\sigma_B(0)$	0.25 mm
Initial number density of felsic crystals, n'_A (z, 0)	36×10^6 m^{-3}
Initial number density of felsic crystals, n'_B (z, 0)	9.5×10^6 m^{-3}
Initial number density of minor constituents, n'_C (z, 0)	0 m^{-3}
Specific heat capacity of melt, c_m	1.09 kJ kg^{-1} K^{-1}
Thermal diffusivity (all substances), κ	7.41×10^{-7} m^2 s^{-1}
Latent heat of fusion for felsic solids, H_A	79.6 kJ kg^{-1}
Latent heat of fusion for mafic solids, H_B	79.6 kJ kg^{-1}
Melt viscosity at reference temperature, μ_0	10^5 Pa s
Reference temperature for viscosity, T_R	655°C
Activation energy for viscosity, Q	153.8 kJ mol^{-1} K^{-1}
Initial Bingham yield stress for melt, τ_0	0 Pa
Steady-state Bingham yield stress for melt, τ_∞	3 Pa
Time constant for melt polymerization, t_B	15 a
Growth rate constant for felsic crystals, V_A	2×10^{-5} Pa m
Growth rate constant for mafic crystals, V_B	2×10^{-5} Pa m
Nucleation rate constant for felsic crystals, $K_A^{(1)}$	2.9×10^{22} m^{-3} s^{-1} K^{-1}
Nucleation rate constant for felsic crystals, $K_A^{(2)}$	3.2×10^5 K^{-3}
Nucleation rate constant for felsic crystals, $K_A^{(3)}$	3.9×10^4 K^{-1}
Nucleation rate constant for mafic crystals, $K_B^{(1)}$	2.9×10^{22} m^{-3} s^{-1} K^{-1}
Nucleation rate constant for mafic crystals, $K_B^{(2)}$	3.2×10^5 K^{-3}
Nucleation rate constant for mafic crystals, $K_B^{(3)}$	3.9×10^4 K^{-1}
Nucleation rate constant for minor constituents, $K_C^{(1)}$	2.9×10^{22} m^{-3} s^{-1} K^{-1}
Nucleation rate constant for minor constituents, $K_C^{(2)}$	3.2×10^5 K^{-3}
Nucleation rate constant for minor constituents, $K_C^{(3)}$	3.9×10^4 K^{-1}
Chemical diffusivity for felsic melt components, $D_A^{(0)}$	5.0×10^{-10} m^2 s^{-1}
Chemical diffusivity for mafic melt components, $D_B^{(0)}$	5.0×10^{-10} m^2 s^{-1}
Chemical diffusivity for minor constituents in melt, $D_C^{(0)}$	5.0×10^{-10} m^2 s^{-1}
Exponent in chemical diffusivity law, v	3
Melt fraction in freshly-settled layer, m_0	0.40
Gravitational acceleration, g	9.8 m s^{-2}
Universal gas constant, R	8.31434 J mol^{-1} K^{-1}

years, even larger mafic and felsic crystals develop adjacent to the melt-dominated upper region.

Figure 6(f & g) provides a time-series perspective. The temporal variations of ϕ_A, ϕ_B, and total solids $\phi_s = \phi_A + \phi_B$ are summarized in Fig. 6(f). Note that the graphs are for the layer-averaged values of solids fraction; this averaging blends values from the solids-rich lower zone and the melt-rich upper zone. Close examination of Fig. 6(f) leads to the conclusion that layer solidification is largely completed by $t = 10$ years. Also plotted in Fig. 6(f) is the temporal variation in the thickness of the region of settled crystals. At $t = 0$, no crystals have settled; by $t = 9$ years, settling is completed and those crystals that have not yet settled cannot do so because they are held in suspension by Bingham forces.

Figure 6(g) shows how the undercooling varies with time and reveals the interplay between melt temperature and melt chemistry. At $t = 0$, the layer is at a temperature of $T_1 = 656$°C, the surroundings are at $T_0 = 652$°C, and the melt liquidus temperature is at $T_L = 656$°C. Very rapidly (too rapidly to resolve in Fig. 6g) the layer temperature drops to the temperature of the surroundings so that melt at the bottom, middle, and top of the layer experiences an undercooling of $\Delta T = 4$°C which drives crystal growth but is insufficient to initiate crystal nucleation. At 3 years, the melt liquidus temperature at the layer bottom has approached the melt temperature and growth of layer-bottom crystals ceases. Growth of layer-middle crystals (i.e. 20 cm above the base) ceases at $t = 15$ years. Although at 25 years the layer-top remains undercooled, the solids growth rate is negligible because there are few crystals present and no additional nucleation centres can appear because the undercooling is insufficient to activate the nucleation process.

The timing of the next layer in the sequence is critical in determining the ratio of the thickness of the fine-grained mafic bottom to the total thickness of the layer (Table 1c). For subsequent discussion, we shall take $\phi_s = 0.7$ to define the mechanical solidus; the thermodynamic solidus condition is, of course, $\phi_s = 1$. At 2 years, the fine-grained mafic bottom reaches its mechanical solidus; only after 10–25 years does the

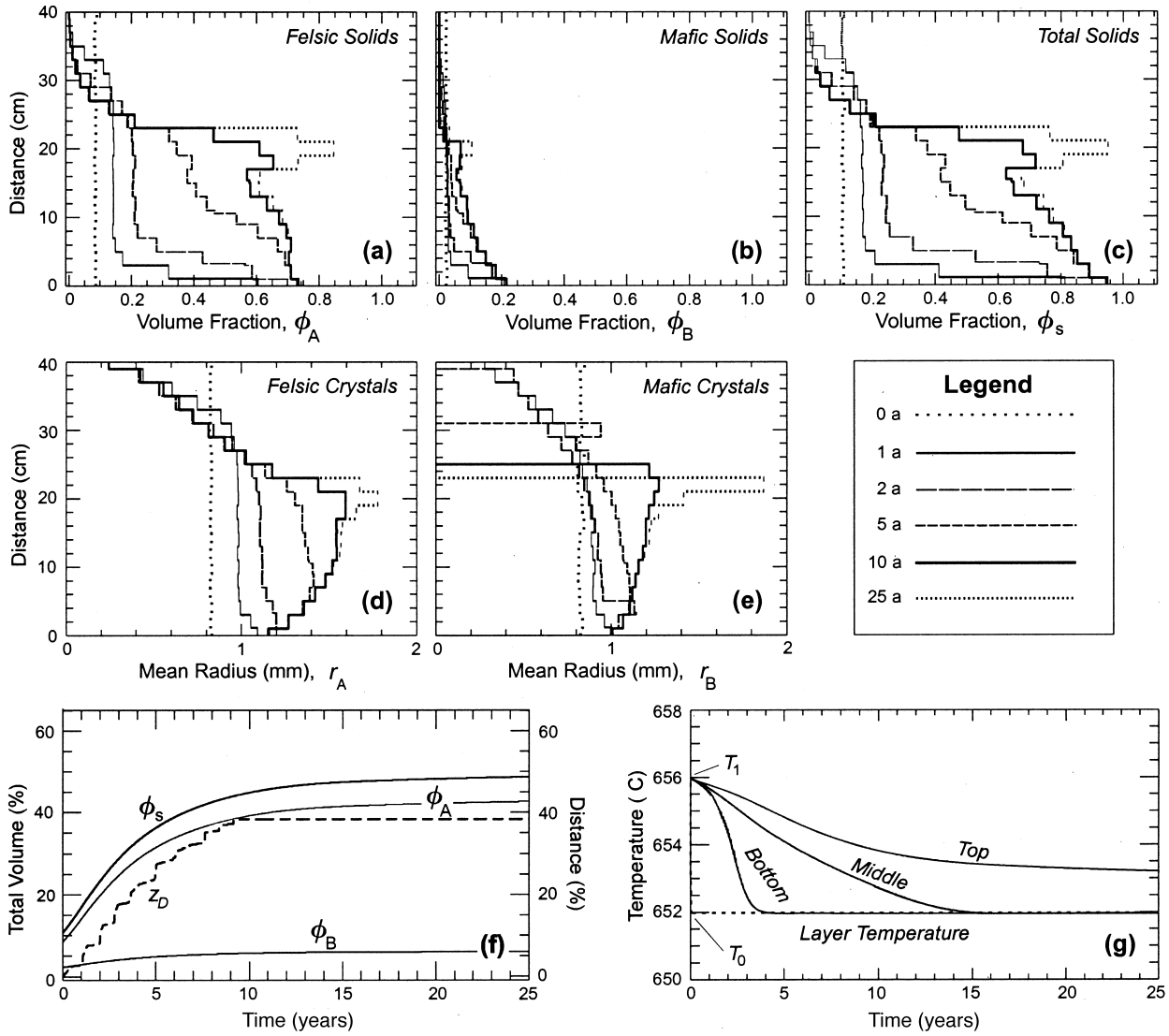

Fig. 6. Results of computational modelling. For the time-slice graphs, results are plotted as histograms rather than as smooth curves, to serve as a reminder that the calculation is based on particle counting. The legend applies only to the time-slice graphs. (a) Time slices showing the spatial variation of felsic solids fraction in a layer. (b) Time slices showing the spatial variation of mafic (biotite) solids fraction in a layer. Note how biotite is concentrated near the layer bottom. (c) Time slices showing the spatial variation of total solids fraction in a layer. (d) Time slices showing the spatial variation of the mean radius of felsic crystals. Note how felsic grain size increases with distance above the layer bottom. (e) Time slices showing the spatial variation of the mean radius of mafic crystals. (f) Time series showing the change in layer-averaged solids fraction for felsic, mafic, and total solids. The dashed line shows the increase in thickness z_D of the sedimented layer with time. For both sets of graphs, results are expressed as a percentage of the total. Note how settling ceases at ~9 years and solidification becomes negligible after 10–25 years. (g) Time series showing the change in layer temperature (dotted line) and melt liquidus temperature (solid lines) for the bottom, middle, and top of the layer. The difference between the liquidus temperature and actual temperature indicates the degree of undercooling.

middle part of the layer reach its mechanical solidus, and the upper part of the layer remains largely melt. If, after 25 years, the next layer now intrudes along the plane of weakness defined by the melt-rich top of the previous layer, only that melt-rich part will be incorporated in the next layer. On the other hand, if the next layer-forming event takes place at, say, only 3 years, neither the upper nor the lower part of the layer will have sufficient mechanical integrity to prevent erosion, and thus scour-and-fill structures should develop locally where layer injection velocities are greatest. Similarly, several relatively rapidly emplaced layers, all with $0.6 < \phi_s < 0.7$, may be disturbed into slump structures as a result of tilting or jostling of the substrate of foliated granodiorite on which they all rest. Perhaps the anomalously thick felsic portion of the uppermost layer is significant in two respects: (i) it never had its melt-rich top removed by a subsequent layer; and (ii) some of that melt-rich material may have flowed diapirically into the overlying foliated granodiorite.

Our model replicates the major mineralogical and textural features of individual layers at Chebucto Head. Currently this model does not take into account proximity effects such as grain clumping, which affects

the Stokes's settling velocity at early stages, or Ostwald ripening, which promotes the growth of large grains at the expense of small ones at later stages (Boudreau, 1994, 1995; Boudreau and McBirney, 1997). Another area for future attention would be to allow the model to treat a sequence of randomly-occurring layer-forming events. For this case, the final state of a single event would establish the initial conditions for the next event.

FORMATION OF THE LAYERED SEQUENCE AT CHEBUCTO HEAD

Unsatisfactory models

Any satisfactory model for the origin of the layered sequence at Chebucto Head should explain as many of the field observations, and operate within as many of the constraints, as possible. To facilitate this process at the outset, we reject: double-diffusive convection because of the foliated K-feldspars, the branching, trough, and slump structures, the confinement of the layers between sharp contacts, and the unidirectional polarity rather than symmetrical development of the layers from the floor and the roof; closed-system deposition from either turbidity currents or two-phase convection because of the restricted height of the layered sequence combined with absence of any detectable cryptic variation [biotites sampled at 15 intervals show $Fe/(Fe + Mg) = 0.69 \pm 0.01$]; metasomatism or granitization of sedimentary rock because the 'sedimentological' features of the layers (bedding thickness, trough structures, grain-size variation) are vastly different from the generally thickly bedded turbiditic metasedimentary host rocks; and shearing of inhomogeneities because of the extreme regularity and repetition of the layers.

As noted by Smith (1975), layering at Chebucto Head shows many similarities to the Twin Peaks granodiorite (Wilshire, 1969). Some of these shared features include: (i) proximity of the layers to the contact with the country rocks; (ii) grain size within individual layers increases as modal biotite decreases; (iii) K-feldspar megacrysts occur only in biotite-rich parts of the layers; (iv) low angle branching of the layers; and (v) modal composition of the layers is equivalent to the surrounding unlayered rocks. The steeply dipping attitude of the layers, coupled with an absence of sharp contacts and any clear relationship to a feeder system, led Wilshire (1969) to conclude that shear flow parallel to the main contact of the intrusion was responsible for the layer formation at Twin Peaks. Smith (1975) also concluded that "episodic shear flow of a suspension of mixed crystal sizes" could explain the layers at Chebucto Head. We suggest that our additional critical field observations at Chebucto Head demand a different interpretation.

New model for the origin of the layers at Chebucto Head

The main features of the layered sequence that must be explained by any acceptable model are the following. (i) The sequence is confined by two sharp, parallel subhorizontal contacts about 8 m apart. (ii) Rhythmic banding, scour-and-fill, and cross-bedding all suggest that the sequence is upright, i.e. the layers were built upwards (or outwards) toward the main contact of the batholith with the country rock. (iii) As indicated by the channelling, slump, and diapiric structures, the layers were not rigid until some time well after their deposition. (iv) The megacrysts and xenoliths that characterize the foliated granodiorite are largely missing from the layers, but are concentrated in the dykes spatially related to the layers. (v) The outer margin of the large megacrystic dyke becomes the first layer of the layered sequence.

We propose the following model to account for most of the observed features in the layered sequence.

Stage I. Immediately preceding the onset of layer formation (Fig. 7a), the following conditions prevailed. (i) A thick margin of foliated granodiorite had congealed against the metasedimentary roof rocks. (ii) Jointing parallel and perpendicular to the contact developed in this region of relatively strong thermal gradients as a result of contraction during cooling of the granodiorite. (At these near-solidus temperatures, the granodiorite should respond brittly to short-term stresses and plastically to long-term stresses.) (iii) The system of joints permitted some parts of the roof to sink or rotate downward into the magma as demanded by density considerations.

Stage II. As a roof block of congealed granodiorite rotates downward, space forms in fractures parallel to the contact (Fig. 7b). Magma must flow up the fracture perpendicular to the batholith–country rock contact and then spread laterally into the fracture parallel to the contact. This injected magma is a sample of the foliated granodiorite and contains silicate melt, microphenocrysts of quartz, feldspar, and biotite, K-feldspar megacrysts, and xenoliths of the metasedimentary country rocks. The system is initially relatively open and three of these constituents (melt, small crystals, and megacrysts) appear to have spread laterally to form the first layers. The xenoliths are probably too large or too dense to travel up the fracture. If the rotation of the subsiding block were episodic, then the interval between layer-forming events must have been sufficiently long to permit gravity sorting of all microphenocrysts and K-feldspar megacrysts in the first layer.

Stages III and IV. Further movements of the block occur after variable intervals of time (Fig. 7c). Depending on the complexity of the fracture system, rotation may take place about a fixed fulcrum, about a moving fulcrum, or by simple downward translation

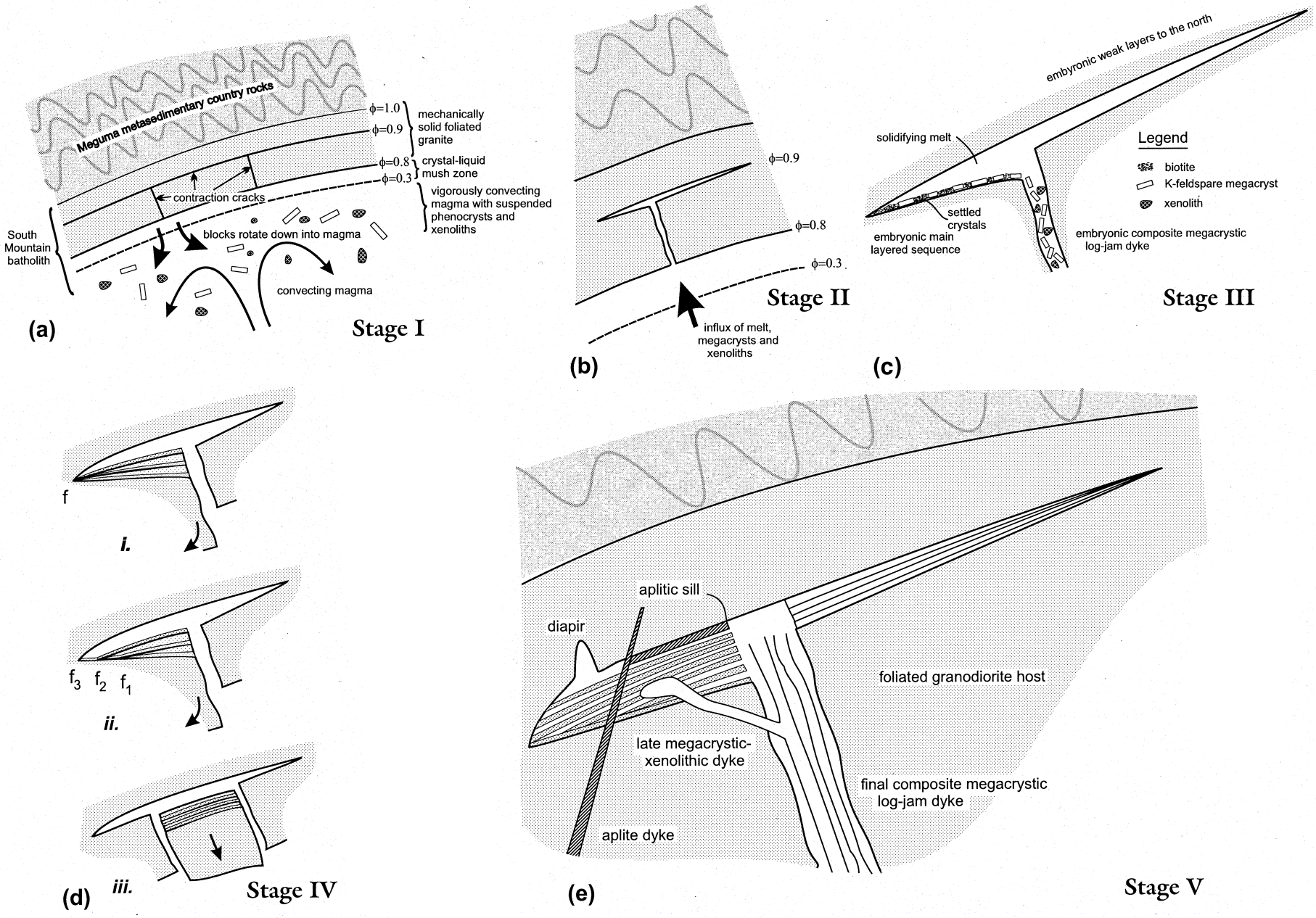

Fig. 7. A pluton-scale model for the development of layers at Chebucto Head. (a) Stage I. Cross-sectional view of the conditions immediately before layer formation begins. (b) Stage II. Melt, megacrysts, and xenoliths are injected into the fracture system in response to the first movement of the roof block. (c) Stage III. Enlargement of the fracture system just after emplacement of the first layer. (d) Stage IV. Three possible types of subsequent block movement: *i.* Fixed-fulcrum rotation producing many layers converging at a point. The dark bases of the layers represent gravity accumulation of biotite-rich material. *ii.* Moving-fulcrum rotation producing bifurcating layers: f_1, f_2, and f_3 are the fulcra for the first three rotations. *iii.* Translation producing many parallel layers. (e) Stage V. Closing stages of layer formation.

(piston faulting) of the block (Fig. 7d). Each of these mechanisms could have taken place and should have different expressions in the layered sequence, particularly in terms of layer bifurcations and slump structures. This process of expansion of the layered body by sinking of its floor is similar to a model proposed by Cruden (1997) for pluton-scale tabular granites.

Assuming that the initial layer is tensionally weakest at its upper surface, where it presumably has the highest concentration of melt (Figs 2k & 6c), the first layer will detach at its upper contact and ride down the subsiding block. New material will then be injected between it and the foliated granodiorite above, the same rock that formed the upper contact of the first layer, with or without some adhering leucocratic material from the previous layer. As shown by the texture of the megacrystic dyke, the fracture feeding the layers becomes choked with megacrysts and xenoliths (a log-jam dyke) that then begins to act as a filter (Propach, 1976) passing only the melt and microphenocrysts into the layered sequence. The proportion of coarse constituents in the layered sequence is greatest in the lowermost few layers and rapidly decreases effectively to zero in the middle and upper layers, except for rare appearances of megacrysts, explained below.

If the times between successive injections are short relative to the time required to solidify the preceding layer, the influx of new material may scour out part of the earliest layer or layers. Also, if the times between new influxes are short, several partly solidified layers may rest upon one another and might be subject to deformation together as the block suddenly moved again on the fracture system. Finally, one other time-dependent phenomenon involves the development of the composite dyke. If the times between pulses were relatively short, each new layer would just tap the top of a standing column of magma, possibly now choked with megacrysts and xenoliths. If the times between pulses were relatively long, the walls of the dyke might be expected to freeze. This solidification would account for the distinct internal contacts in the dyke, for the sporadic appearance of megacrysts at random heights in the layered sequence as a new fracture is opened, for the general absence of xenoliths in the layers because they sank in the composite dyke, and for the fact that the number of zones in the dyke does not have to be the same as the number of layers in the layered sequence.

The composite dyke is also very interesting geometrically. When the dyke first formed, it extended to the top of the contact-parallel fracture. As the walls subsided and the layers developed, the dyke continued to extend to the same height, and that level then became the permanent roof of the layered sequence. This being the case, as a structural feature the dyke is actually *older* than the layers it appears to cut, even though some of the material in its interior is younger. The absence of shearing along the margin of the dyke logically suggests that the strain associated with the dropping block was accommodated in its mushy interior.

Stage V. Eventually, with only a total displacement of 8 m on the fracture occupied by the composite dyke, the process of layer formation ceased. Before the system became entirely rigid several minor events seem to have occurred (Fig. 7e). First, injection of many pulses of magma into the layers resulted in heating the formerly rigid, overlying, granodiorite to the point where hot, less viscous material could rise diapirically out of the layers, such as the load structures in Strzegom granites (Puziewicz and Wojewoda, 1984), and in the Rhum ultramafic intrusion (Volker and Upton, 1990). Second, the area was subjected to injection of aplites, that were unrelated to the main composite dyke, before the upper contact of the layered sequence had completely solidified. The aplitic material exploited the same plane of weakness, i.e. the top of the layered sequence, that the magmas from the composite dyke had earlier exploited, and were injected as sills in that position. Finally, and most speculatively, buoyantly rising bodies of material, rich in megacrysts and xenoliths, possibly from the composite dyke, penetrated the layered sequence (Fig. 2p), in a style similar to that of the late wehrlite pipes in the Rhum intrusion (Volker and Upton, 1990). Because xenoliths are absent from the layered sequence, and rare in the exposed part of the megacrystic dyke, we suggest that a possible source of megacrysts and xenoliths for these late cross-cutting diapiric bodies is in the lower reaches of the composite dyke. The diapir/dyke itself (Fig. 2p) shows what may be gravity sorting of xenoliths (lower) and megacrysts (upper) that we propose for the main composite dyke. That these diapiric bodies are cross-cutting to concordant suggests they are late in the intrusive history of the layered sequence, notwithstanding the previous conclusion regarding the age of the composite megacrystic dyke.

CONCLUSIONS

Well-developed layering is rare in granitic rocks and, where it occurs, its origin is always enigmatic (Parsons, 1987, pp. 419–423). Rhythmic layering, similar to that at Chebucto Head, occurs near the margins of many other batholiths world-wide. Normally, however, the subhorizontal fracture containing the layers has annealed to such an extent that the layers merely resemble isolated schlieren zones. Also, if the complementary megacrystic feeder dykes are not exposed, then accurate interpretation of the origin of such layers is difficult or impossible.

By contrast, the excellent exposures at Chebucto Head have permitted us to deduce the physical and chemical processes that may have formed the layered sequence. The excellent development of grain-size and modal layering, the pseudo-sedimentary structures,

and the megacrystic feeder dykes all provide an opportunity to model these features. We believe that the layers resulted from the repeated motion of a block of congealed granodiorite, cooling and contracting in the steep thermal gradients of the outer part of the batholith and subsiding into the main magma, by the injection of magma into the resulting fractures above and bounding the subsiding block. Although no one-for-one relationship exists between the layers and the zones in the composite megacrystic feeder dyke, conceptually the layers are nevertheless like any composite dyke or sheeted dyke complex, i.e. subsequent intrusions occur along the weakest portion. In a composite dyke, the weakest portion is the central portion; in a composite sill undergoing crystal settling, it is the most molten upper portion. In our model, we have replicated the variation in mineral proportions and grain sizes, and shown that crystals can settle before the layer solidifies, thereby permitting rhythmic layers to be generated for each pulse. Furthermore, the 10–25 year solidification times predicted by the model provide an opportunity for further movement on the substrate to cause deformation of pre-existing layers, and for subsequent injections of magma to erode partially consolidated previous layers.

We believe that this interpretation of emplacement of a layered sequence above a subsiding block of solidifying granitic material in the outer margin of the batholith is generally applicable to other occurrences of such layering. We also believe that our mathematical model is applicable to a variety of other rhythmically layered igneous rocks.

Acknowledgements—This research was supported by grants from the Natural Sciences and Engineering Research Council of Canada. D. D. Trent and E-an Zen made extremely helpful comments on a much earlier version of this manuscript. This paper is dedicated to our parents who took a special interest in the progress of this work.

REFERENCES

Abbott, R. N. (1989) Internal structures in part of the South Mountain batholith, Nova Scotia, Canada. *Geological Society of America Bulletin* **101,** 1493–1506.

Abbott, R. N. and Clarke, D. B. (1979) Hypothetical liquidus relationships in the system Al_2O_3–FeO–MgO projected from quartz, alkali feldspar and plagioclase for $a(H_2O) \leq 1$. *Canadian Mineralogist* **17,** 549–560.

Balk, R. (1937) *Structural Behaviour of Igneous Rocks*. Memoirs of the Geological Society America **5**.

Barrière, M. (1981) On curved laminae, graded layers, convection currents and dynamic crystal sorting in the Ploumanac'h (Brittany) subalkaline granite. *Contributions to Mineralogy and Petrology* **77,** 214–224.

Berry, R. F. and Flint, R. B. (1988) Magmatic banding within Proterozoic granodiorite dykes near Streaky Bay, South Australia. *Transactions of the Royal Society of South Australia* **112,** 63–73.

Bhattacharji, S. and Smith, C. H. (1964) Flowage differentiation. *Science* **145,** 150–153.

Boudreau, A. E. (1994) Mineral segregation during crystal aging in two-crystal, two-component systems. *South African Journal of Geology* **97,** 473–485.

Boudreau, A. E. (1995) Crystal aging and the formation of fine-scale igneous layering. *Mineralogy and Petrology* **54,** 55–69.

Boudreau, A. E. and McBirney, A. R. (1997) The Skaergaard layered series: Part III. Non-dynamic layering. *Journal of Petrology* **38,** 1003–1020.

Brandeis, G., Jaupart, C. and Allègre, C. J. (1984) Nucleation, crystal growth and the thermal regime of cooling magmas. *Journal of Geophysical Research* **89,** 10,161–10,177.

Brown, P. E., Chambers, A. D. and Becker, S. M. (1987) A large soft-sediment fold in the Lilloise intrusion, East Greenland. In *Origins of Igneous Layering*, ed. I. Parsons, pp. 125–143. NATO Advanced Research Workshop, Narsarsuaq, South Greenland (August 4–15, 1986), NATO Advanced Science Institute Series C, Mathematical and Physical Sciences, D. Reidel, Amsterdam.

Cawthorn, R. G. (1996) *Layered Intrusions*. Elsevier, New York.

Clarke, D. B. (1980) The South Mountain batholith. In *Field Trip Guidebook, Trip 21: Igneous and Metamorphic Geology of Southern Nova Scotia*, ed. D. B. Clarke and C. K. Muecke, pp. 12–47. Geological Association of Canada–Mineralogical Association of Canada.

Clarke, D. B. and Muecke, G. K. (1985) Review of the petrochemistry and origin of the South Mountain Batholith and associated plutons, Nova Scotia, Canada. In *High Heat Production (HHP) Granites, Hydrothermal Circulation Circulation and Ore Genesis*. The Institution of Mining and Metallurgy, London, pp. 41–54.

Cruden, A. R. (1997) On the emplacement of tabular granites. *Journal of the Geological Society of London* **155,** 852–862.

Dowty, E. (1980) Crystal growth and nucleation theory and the numerical simulation of igneous crystallization. In *Physics of Magmatic Processes*, ed. R. D. Hargraves, pp. 419–485. Princeton University Press, Princeton.

Duke, E. F., Redden, J. A. and Papike, J. J. (1988) Calamity Peak layered granite–pegmatite complex, Black Hill, South Dakota: Part I. Structure and emplacement. *Geological Society of America Bulletin* **100,** 825–840.

Fowler, D. L., Friend, L. D., Yanicak, S. M. and Ericson, R. C. (1986) *Petrology and structure of a rhythmically layered granodiorite sequence near Mt. Clark, Yosemite National Park, California*. Abstracts with Programs of the Geological Society, America **18,** 106.

Harry, W. T. and Emeleus, C. H. (1960) Mineral layering in some granitic intrusions of S. W. Greenland. *International Geological Congress, Report of the Twenty-First Session Norden* **XIV,** 172–181.

Hort, M., Marsh, B. D. and Spohn, T. (1993) Igneous layering through oscillatory nucleation and crystal settling in well-mixed magmas. *Contributions to Mineralogy and Petrology* **114,** 425–440.

Irvine, T. N. (1987a) Appendix I. Glossary of terms for layered intrusions. In *Origins of Igneous Layering*, ed. I. Parsons, pp. 641–647. NATO Advanced Research Workshop, Narsarsuaq, South Greenland NATO Advanced Science Institute Series C, Mathematical and Physical Sciences. D. Reidel, Amsterdam.

Irvine, T. N. (1987b) Appendix II. Processes involved in the formation and development of layered igneous rocks. In *Origins of Igneous Layering*, ed. I. Parsons, pp. 649–656. NATO Advanced Research Workshop, Narsarsuaq, South Greenland NATO Advanced Science Institute Series C, Mathematical and Physical Sciences. D. Reidel, Amsterdam.

Jackson, K. A. (1967) Current concepts in crystal growth from the melt. *Progress in Solid State Chemistry* **4,** 53–80.

Lamb, H. (1963) *Hydrodynamics*. Sixth edition Cambridge University Press, Cambridge.

MacDonald, M. A. (1981) The mineralogy, petrology and geochemistry of the Musquodoboit batholith. M.Sc. thesis, Dalhousie University, Halifax, Novia Scotia.

Malvern, L. E. (1969) *Introduction to the Mechanics of Continuous Media*. Prentice-Hall, Englewood Cliffs.

Marre, J. (1986) *The Structural Analysis of Granitic Rocks*. Elsevier, New York.

Maude, A. D. and Whitmore, R. L. (1958) A generalized theory of sedimentation. *British Journal of Applied Physics* **9,** 477–482.

Naslund, H. R. and McBirney, A. R. (1996) Mechanisms of formation of igneous layering. In *Layered Intrusions*, ed. R. G. Cawthorn, pp. 1–43. Elsevier, Amsterdam.

Parsons, I. (1987) In *Origins of Igneous Layering*. NATO Advanced Research Workshop, Narsarsuaq, South Greenland (August 4–15, 1986), NATO Advanced Science Institute Series C. Mathematical and Physical Sciences. D. Reidel, Amsterdam.

Paterson, S. R., Vernon, R. H. and Tobisch, O. T. (1989) A review of criteria for the identification of magmatic and tectonic foliations in granitoids. *Journal of Structural Geology* **11,** 349–363.

Peterson, J. W. and Newton, R. C. (1988) Reversed experiments on biotite–quartz–feldspar melting in the system KMASH: implications for crustal anatexis. *Journal of Geology* **97,** 465–485.

Propach, G. (1976) Models of filter differentiation. *Lithos* **9,** 203–209.

Puziewicz, J. and Wojewoda, J. (1984) Origin of load structures and graded beddings of dark minerals in the Strzegom granites (SW Poland)—a sedimentological and petrological approach. *Neues Jahrbuch für Mineralogie Monatshefte*, pp. 353–363.

Richtmyer, R. D. and Morton, K. W. (1967) *Difference Methods for Initial-Value Problems. Second Edition.* Interscience Publishers, New York.

Rodriguez, F. (1982) *Principles of Polymer Systems.* McGraw-Hill, New York.

Sisson, T. W., Moore, J. G. and Czamanske, G. K. (1988) Cumulates, flame rock, and banded aplites at the top of a typical Sierran granodiorite, Emerald Lake, California. *EOS, Transactions of the American Geophysical Union* **69,** 1490.

Smith, T. E. (1975) Layered granitic rocks at Chebucto Head, Halifax County, Nova Scotia. *Canadian Journal of Earth Sciences* **12,** 456–463.

Stephenson, P. J. (1990) Layering in felsic granites in the main East pluton, Hinchinbrook Island, North Queensland, Australia. *Geological Journal* **25,** 325–336.

Truesdell, C. and Toupin, R. (1960) The classical field theories. In *Encyclopedia of Physics*, ed. S. Flügge, Vol. 3/1, pp. 226–793. Springer-Verlag, Berlin.

Turnbull, D. and Fischer, J. C. (1949) Rate of nucleation in condensed systems. *Journal of Chemical Physics* **17,** 71–73.

Vielzeuf, D. and Holloway, J. R. (1988) Experimental determination of the fluid-absent melting relations in the pelitic system. Consequence for crustal differentiation. *Contributions to Mineralogy and Petrology* **98,** 257–276.

Volker, J. A. and Upton, B. G. J. (1990) The structure and petrogenesis of the Trallval and Ruinsival areas of the Rhum ultrabasic complex. *Transactions of the Royal Society, Edinburgh: Earth Sciences* **81,** 69–88.

Wager, L. R. and Brown, G. M. (1967) *Layered Igneous Rocks.* Oliver and Boyd, Edinburgh.

Wilshire, H. G. (1969) Mineral layering in the Twin Lakes granodiorite, Colorado. *Memoirs of the Geological Society, America* **115,** 235–261.

Woodend-Douma, S. L. (1988) The mineralogy, petrology and geochemistry of the Port Mouton pluton, Nova Scotia, Canada. M.Sc. thesis, Dalhousie University, Halifax, Nova Scotia.

APPENDIX A

Particle settling

Stokes's law for the velocity v_p of an isolated spherical particle of radius r_p and density ρ_p settling in a fluid of density ρ_m and viscosity μ is obtained by equating the viscous drag force $F_D = 6\pi\mu r_p v_p$ to the buoyancy-compensated gravitational force $F_G = 4/3\pi(\rho_p - \rho_m) g r_p^3$ to obtain the familiar result

$$v_p = \frac{2}{9\mu}\left(\rho_p - \rho_m\right) g r_p^2. \tag{A1}$$

In our model we take felsic crystals to be spherical but, for calculating the settling of biotite crystals, we approximate the crystals as circular disks. Lamb (1963, pp. 604–605) shows that, for a circular disk having radius r_p, the drag force ranges between the limiting values $F_D = 32/3\ \mu r_p v_p$ (for edgeways settling) and $F_D = 16\ \mu r_p\ v_p$ (for broadside-on settling). For our models the particle Reynolds number, defined as $Re_p = 2\rho_m r_p\ v_p/\mu$, is extremely low; thus a freely-settling crystal will remain in its initial orientation. Rather than concern ourselves with tracking the orientation of individual crystals, we take the geometric mean of the two drag equations to obtain a representative value $F_D = 13.06\ \mu r_p\ v_p$. For a disk having thickness $\Delta d = \Gamma r_p$ (where Γ is the thickness-to-radius ratio for the disk), the gravitational force is $F_G = \Gamma\pi(\rho_p - \rho_m) g r_p^3$. Equating the drag and gravitational forces gives the disk settling rule

$$v_p = \frac{\Gamma\pi}{13.06\mu}\left(\rho_p - \rho_m\right) r_p^2; \tag{A2}$$

for biotite crystals, we take $\Gamma = \frac{1}{2}$.

The effects of Bingham behaviour can be approximated by introducing a second resistive force $F_B = \tau S_p$ where τ is the magnitude of the Bingham yield stress and S_p is the surface area of the particle ($S_p = 4\pi r_p^2$ for a sphere and $S_p = 2\pi r_p^2(1 + \Gamma)$ for a circular disk). Incorporating the Bingham force in the force balance equation and reworking the settling analysis gives the result

$$v_p = \begin{cases} v_p^S - v_p^B & v_p^S > v_p^B \\ 0 & v_p^S \le v_p^B \end{cases} \tag{A4}$$

where

$$v_p^S = \begin{cases} \dfrac{2}{9\mu}\left(\rho_p - \rho_m\right) g r_p^2 & \text{for spheres} \\ \dfrac{2\pi(1+\Gamma)\tau r_p}{13.06\mu} & \text{for orientation-averaged disks} \end{cases} \tag{A5}$$

and

$$v_p^B = \begin{cases} \dfrac{2\tau r_p}{3\mu} & \text{for spheres} \\ \dfrac{2\pi(1+\Gamma)\tau r_p}{13.06\mu} & \text{for orientation-averaged disks} \end{cases}. \tag{A6}$$

Finally, we introduce grain-cluttering effects by replacing the true melt viscosity μ by an effective viscosity (Maude and Whitmore, 1958)

$$\mu_E = \begin{cases} \mu/m^{4.65} & m > m_0 \\ \mu/m_0^{4.65} & m \le m_0 \end{cases} \tag{A7}$$

where $m_0 = 1 - \phi_0$ is taken as the melt concentration that corresponds to the solids packing density ϕ_0 in a newly-sedimented layer.

APPENDIX B

Polymerization and Bingham stress

The following rate theory is proposed to provide a simple justification for our assumed time dependence of the Bingham yield stress. Suppose that melt polymerization is governed by the following one-step chemical reaction

$$X \rightleftharpoons Y \tag{B1}$$

where X represents an unpolymerized molecule and Y a polymerized one. Assuming first-order kinetics, the chemical evolution is described by

$$\frac{dc_X}{dt} = -k_f c_X + k_r c_Y \tag{B2a}$$

$$\frac{dc_Y}{dt} = +k_f c_X - k_r c_Y. \tag{B2b}$$

To focus attention on the reaction product Y, we write $c_X = c_{X0} + c_{Y0} - c_Y$ where c_{X0} and c_{Y0} are the initial concentrations of X and Y. Applying this substitution to (B2) and solving the differential equation gives

$$c_Y(t) = \frac{k_r(c_{X0} + c_{Y0})}{k_f + k_r} + \left(\frac{k_r c_{Y0} - k_f c_{X0}}{k_f + k_r}\right) \exp\left[-(k_f + k_r)t\right]. \tag{B3}$$

We postulate that the Bingham yield stress is proportional to the concentration of polymers, thus

$$\tau = B c_Y \tag{B4}$$

where B is a proportionality constant. Substituting (B4) directly into (B3) yields the result

$$\tau(t) = \frac{k_f(B c_{X0} + \tau_0)}{k_f + k_r} + \left(\frac{k_r\tau_0 - B k_f c_{X0}}{k_f + k_r}\right) \exp[-(k_f + k_r)t] \tag{B5}$$

where $\tau_0 = \tau(0)$. With the definitions $(\tau_\infty) = \tau(\infty) = k_f\ (B c_{A0} + \tau_0)/$

(k_f+k_r) and $t_B=1/(k_f+k_r)$ expression (B5) reduces to

$$\tau(t)=\tau_\infty+(\tau_0-\tau_\infty)\exp(-t/t_B). \tag{B6}$$

APPENDIX C

Chemical evolution

Letting the chemical components be denoted by the subscript α where $\alpha = A,B,C\ldots$, we define M_α as the volume of melt component α contained in volume V; thus

$$M_\alpha=\int_V mc_\alpha\,\mathrm{d}^3r \tag{C1}$$

where m is the melt fraction and c_α is the volume concentration of melt constituent α. Applying the Reynolds transport theorem (e.g. Malvern, 1969, pp. 210–211) to equation (C1) gives

$$\frac{\mathrm{d}M_\alpha}{\mathrm{d}t}=\int_V\frac{\partial}{\partial t}(mc_\alpha)+\nabla\cdot(mc_\alpha\mathbf{v}_m)\,\mathrm{d}^3r \tag{C2}$$

where $\mathbf{v}_m$ is the melt velocity. The general balance theorem (e.g. Truesdell and Toupin, 1960, pp. 468) applied to M_α gives the global-form balance expression

$$\frac{\mathrm{d}M_\alpha}{\mathrm{d}t}=-\int_V\nabla\cdot\mathbf{J}_\alpha\,\mathrm{d}^3r-\int_V\Phi_\alpha\,\mathrm{d}^3r \tag{C3}$$

where $\mathbf{J}_\alpha$ is the diffusion flux of chemical component α in the melt phase and Φ_α is the volume rate of production of *solid* component α from the melt. Equating (C4) and (C3) gives

$$\frac{\partial}{\partial t}(mc_\alpha)+\nabla\cdot(mc_\alpha\mathbf{v}_m)=-\nabla\cdot\mathbf{J}_\alpha-\Phi_\alpha. \tag{C4}$$

Expanding the left-hand side of (C4) and applying (C3) gives the local-form balance for melt component α

$$m\left(\frac{\partial c_\alpha}{\partial t}+\mathbf{v}_m\cdot\nabla c_\alpha\right)+c_\alpha\Phi_m=-\nabla\cdot\mathbf{J}_\alpha-\Phi_\alpha \tag{C5}$$

with

$$\Phi_m=-\sum_\alpha\Phi_\alpha \tag{C6}$$

(because the rate of production of solids matches the rate of disappearance of melt). In order to understand the implications of (C5) it is important to comprehend the nature of the production terms $c_\alpha\Phi_m$ and Φ_α. The first term describes the effect of changing melt volume *without changing the total amount of component α in the melt*; for this case, reduction of melt volume increases the concentration of α. The second term is associated with the removal of α from the melt, which reduces c_α.

The diffusive flux of melt component α is assumed to be governed by Fick's law

$$\mathbf{J}_\alpha=-D_\alpha\nabla c_\alpha \tag{C7}$$

where D_α is the chemical diffusivity of melt constituent α. The chemical diffusivity is expected to decrease with decreasing melt fraction; thus we write

$$D_\alpha=D_\alpha^{(0)}m^\nu \tag{C8}$$

where $D_\alpha^{(0)}$ is the diffusivity in 100% melt and ν is a positive exponent. Combining equations (C5)–(C8) gives the chemical balance equation

$$m\left(\frac{\partial c_\alpha}{\partial t}+\mathbf{v}_m\cdot\nabla c_\alpha\right)=+\nabla\cdot\left(D_\alpha^{(0)}m^\nu\nabla c_\alpha\right)-\Phi_\alpha+c_\alpha\sum_\alpha\Phi_\alpha. \tag{C9}$$

Equation (C9) applies to each melt component but, because $c_A+c_B+c_C=1$, it is only necessary to solve for any two of the components.

APPENDIX D

Particles and fields

We consider an ensemble of N particles numbered sequentially from $p = 1\ldots N$. The mineral type of each particle is tagged by a character variable $e_p=\alpha$ = A, B, C and, to permit counting of the different types of particles, we introduce an indicator function having the following properties:

$$\delta_{\alpha e_p}=\begin{cases}1 & \text{if } \alpha=e_p\\ 0 & \text{otherwise}\end{cases}. \tag{D1}$$

The behaviour of $\delta_{\alpha e_p}$ is suggestive of a Kronecker delta; for example, if particle p is of crystal type A, then $e_p=$A, $\delta_{Ae_p}=1$ and $\delta_{Be_p}=\delta_{Ce_p}=0$. The delta function is useful for attaching properties to individual particles, for example if particle p is of crystal type α then it follows that its density is $\rho_p=\Sigma_\alpha\delta_{\alpha e_p}\rho_\alpha=\rho_A$.

We are interested in describing the collective behaviour of particles that are initially distributed over a fluid layer of thickness h. For calculation purposes, we introduce a box-like volume $V = Ah$ where $A = L_xL_y$ is the base area and L_x and L_y are fictive length and width dimensions. For each solid phase α, the initial number density, particle size distribution, and spatial distribution functions are specified as input data. Subject to these constraints, a random number generator is employed to assign values for the chemistry e_p, spatial position (x_p, y_p, z_p), and radius r_p of each particle in the ensemble. Once these attributes have been set, the layer is divided into horizontal lamina of thickness Δz_i such that for typical cells (i.e. not near boundaries and not near any internal discontinuity surfaces) the lamina is centred at $z = z_i$ and hence bounded below and above at $z = z_i-1/2\Delta z$ and $z = z_i+1/2\Delta z$. By this process we generate subregions having volume $V_i=A\Delta z_i$ with the properties $h = \Sigma_i\ \Delta z_i$ and $V = \Sigma_i\ V_i$. For simplicity we denote the subregion having volume V_i as Z_i and introduce the notation $z\in Z_i$ to indicate that a particular value of z lies inside this region. (The symbol $\in$ is conventionally used to indicate that a quantity 'belongs to' or 'is a member' of a particular class.) We employ this notation to indicate particle p of the ensemble lies within the region Z_i as follows: $z_p\in Z_i$. Thus the total number of particles and the total number of α-phase particles are, respectively, given as

$$\sum_\alpha\sum_{z_p\in Z_i}\delta_{\alpha e_p}=N_i\quad\text{and}\quad\sum_{z_p\in Z_i}\delta_{\alpha e_p}=N_{\alpha i}. \tag{D2}$$

Additionally

$$\sum_p\delta_{\alpha e_p}=N,\ \sum_i N_i=N,\ \sum_i N_{\alpha i}=N_\alpha,\ \text{and}\ \sum_\alpha N_\alpha=N, \tag{D3}$$

where N is the total number of particles and N_α is the total number of α-phase particles.

The number density of particles having crystal type α is denoted by $n'_\alpha(z,t)$. This function can be readily estimated using the known positions and mineral type of the ensemble of N particles. We employ the approximation to obtain

$$n'_\alpha(z_i,t)=\frac{1}{\Delta V_i}\sum_{z_p\in Z_i}\delta_{\alpha e_p}. \tag{D4}$$

Following a similar approach, we form expressions for the volume fraction, volume flux, and volume rate of production of solid phase α:

$$\phi_\alpha(z_i,t)=\frac{4\pi}{3\Delta V_i}\sum_{z_p\in Z_i}\delta_{\alpha e_p}r_p^3 \tag{D5a}$$

$$J_\alpha(z_i,t)=\frac{4\pi}{3\Delta V_i}\sum_{z_p\in Z_i}\delta_{\alpha e_p}v_pr_p^3 \tag{D5b}$$

$$\Phi_\alpha(z_i,t)=\frac{4\pi}{\Delta V_i}\sum_{z_p\in Z_i}\delta_{\alpha e_p}r_p^2\frac{\mathrm{d}r_p}{\mathrm{d}t} \tag{D5c}$$

where v_p is the particle velocity, determined from equation (1) and $\mathrm{d}r_p/\mathrm{d}t$ is evaluated using the crystal growth equation (4). The rate of accretion of the settled layer is calculated from the volume flux of

solids $J_s = J_A + J_B + J_C$ and the assumed sedimentary packing density $\phi_0 = 1 - m_0$.

Nucleation of condensation centres is governed by equation (5) and leads to addition of new particles, having appropriate mineral chemistry and initial radius $r_p(0) = 0$, at random spatial positions within a given subregion Z_i. If nucleation is occurring, the value of N increases as time increases.